Journal of Applied Fluid Mechanics, Vol. 14, No. 2, pp. 601-613, 2021.
Available online at www.jafmonline.net, ISSN 1735-3572, EISSN 1735-3645.
DOI: 10.47176/jafm.14.02.31567

Mixing and Interpenetration in a Three-Dimensional Buoyancy-Driven Flow of Two Immiscible Liquids: A GPU Based LBM Approach

P. R. Redapangu†, T. G. Kidan and K. Berhane

Department of Chemical Engineering, Ethiopian Institute of Technology - Mekelle (EIT-M), Mekelle University, Ethiopia

†*Corresponding Author Email*: *prasanna.rani@mu.edu.et*

(Received March 5, 2020; accepted July 17, 2020)

ABSTRACT

The Buoyancy-driven flow of two immiscible liquids having varying density and viscosity is studied in a three-dimensional inclined confined channel. Initially, the heavier/lighter liquids occupy the upper/lower parts of the channel, respectively, which is an unstable configuration. The numerical simulations are performed using a multiphase lattice Boltzmann method (LBM) that is further implemented on the graphics processing unit (GPU). The three-dimensional flow dynamics and the associated physics are studied based on various parameters such as viscosity ratios (m), Atwood numbers (At) and Reynolds numbers (Re). The results were presented in the form of iso-surface/contour plots, average density profiles, and lengths of interpenetration. It is observed that larger interpenetration occurs with iso-viscous liquids having higher density gradients (higher At). The Reynolds number had a non-monotonic effect on the axial lengths of interpenetration (Lp^*); Lp^* increases till Re = 500 and then decreases for Re = 1000. At larger Re, due to the development of Kelvin-Helmholtz instabilities higher transverse interpenetration is observed.

Keywords: Buoyancy-driven flow; Length of interpenetration; Immiscible fluids; Kelvin-Helmholtz instabilities; Lattice Boltzmann method.

1. INTRODUCTION

Two fluids, heavier/lighter, situated in a confined channel interpenetrate into each other when subjected to gravitational constraint. Initially, the fluids were separated by an obstruction which then is suddenly removed allowing the fluids to mix. Such a flow is referred as buoyancy-driven/gravitydriven or lock-exchange flow Benjamin (1968), Wood (1970), Séon *et al*. (2004). The investigation of this kind of flow is useful in understanding the physics and dynamics in various fields of science such as ocean and atmospheric science modeling, geophysical flows (example, avalanches) as well as many chemical engineering unit operations and processes. Thus, this problem had attracted wide researchers to perform experimental as well as numerical studies over wide parametric conditions Debacq *et al*. (2001), Séon *et al*.(2004), Séon *et al*. (2005), Hallez and Magnaudet (2008), Birman *et al*. (2007) Redapangu *et al*. (2012a), Sahu and Vanka (2011), Redapangu and Sahu (2013). The present paper presents an investigation on the mixing/interpenetration characteristics of the buoyancy-driven flow of two immiscible liquids in a three-dimensional tilted channel.

Most experiments carried out by various research groups to study the mixing characteristics in the lock-exchange flows were done by mainly considering miscible fluids of different densities Debacq *et al*. (2001), Fernandez *et al*. (2002), Debacq *et al*. (2003), Séon *et al*. (2004) , Séon *et al*. (2005), Séon *et al*. (2007a). Studies of Debacq *et al*. (2001) provided three regimes of flow behavior for a wide range of Atwood numbers. Experiments of Séon *et al*. (2004), Séon *et al*. (2005), Séon *et al*. (2006), Séon *et al*. (2007a), Séon *et al*. (2007b), also provided mixing characteristics and three flow regimes based on the tilt angle, θ, being measured with the vertical.

The interpenetration of the two fluids was observed to be characterized by a diffusive process when the confined geometry is oriented closer towards vertical ($\theta < 65^\circ$). In a tilted geomtery where the gravitational force has two non-zero components, the axial component induces mixing and the interface becomes unstable that gives rise to Kelvin-

Helmholtz instabilities. The mixing also depends on the properties of the fluids, some flows involve low density ratios and some high density ratios. For a near horizontal pipe ($\theta > 85^{\circ}$), the fluids move oppositely as Poiseulle flows, in which the front velocities and the mixing are resultant of the balance of buoyancy and wall friction. In the intermediate region, the front velocity of the flow was observed to be constant and depends on fluid viscosity. Constant front velocity in the intermediate range of tilt angles was also observed by Hallez and Magnaudet (2008) for various Atwood and Reynolds numbers.

Computational studies related to the present topic of interest were also carried out by many investigators using various computational approaches. Birman *et al*. (2005), Birman *et al*. (2007) solved the Navier-Stokes equations using spectral and finite difference methods by considering the fluids with high density contrast. Using finite volume method, Hallez and Magnaudet (2008), Hallez and Magnaudet (2009) studied the mixing characteristics based on various parameters. They also compared the mixing characteristics in various geometries involving two-dimensional (2-D) and three-dimensional (3-D) flows. They stated that the flow and the behavior of instabilities are different in 2-D to that of 3-D flows. In a non-isothermal field, Wakale *et al*. (2015) solved Navier-Stokes equations to study the effects of Bond number, Marangoni number, Reynolds number, density ratio and viscosity ratio. The authors compared the flow dynamics and instabilities in isothermal and non-isothermal systems. Lee and Kim (2013) considered the buoyancy-driven flow of multiple immiscible fluids in a titled channel and investigated how the interface dynamics behave in such a configuration.

A new and promising numerical approach for simulation of interfacial flows, the lattice Boltzmann method (LBM), has been developed and used by many researchers in wide areas of interests Succi *et al*. (1991), Shan and Chen (1993), Shan and Doolen (1995), Chen *et al*. (1996), Premnath and Abraham (2005), Fakhari and Rahimian (2009), Fakhari and Rahimian (2010), Chang and Alexander (2006), Redapangu *et al*. (2013), Redapangu *et al*. (2012b), Rahmati *et al*. (2014), Rahmati and Najjarnezami (2016), Li *et al*. (2020). With respect to the current field of investigation, Sahu and Vanka (2011) developed the multiphase LBM for simulating immiscible fluids based on the multiphase approach proposed by He *et al*. (1999a), He *et al*. (1999b), Zhang *et al*. (2000) and used it to study the buoyancy-driven flow of two immiscible fluids of same viscosities with wide density ratios. This LBM solver was validated with both finite volume Ding *et al*. (2007) and experimental results Séon *et al*. (2004). Major investigations carried in their work were on the change of front velocities with respect to Atwood number, Reynolds number, tilt angles and surface-tension. Based on this solver, Redapangu *et al*. (2012a) then investigated the problem further by considering the immiscible fluids of different viscosities and densities. The main investigations of this study were to find out the effects of viscosity gradients on flow structures and corresponding front velocities. Comparitive studies of 2-D and 3-D of these flows are performed by Redapangu and Sahu (2013) to find the similarities or the contrasts in the dynamics and behavior of instabilities in such flows. Their observations regarding 2-D and 3-D instabilities were found in good agreement with Oliveira and Meiburg (2011) who performed Navier-Stokes simulations to study miscible displacements in Hele-Shaw cells.

As discussed above, most of the studies on buoyancy-driven flows are carried out on 2-D geometries. Therefore the present study focuses on the 3-D investigations of buoyancy-driven flow of two immiscible liquids using lattice Boltzmann method. The two immiscible liquids considered in this study are of varying viscosity and density. The present study is considerably different from our previous works, where 2-D simulations of the buoyancy-driven flows Redapangu *et al*. (2012a) and 3-D simulations of the displacement flows Redapangu and Sahu (2013) are studied using various parametric conditions. In displacement flows, the flow is a resultant of the induced pressure-gradient at the inlet. In the present study, the main objective is to investigate the mixing/interpenetration dynamics of lock-exchange flow in a three-dimensional channel. The study is carried out based on mainly three parameters, the viscosity ratio (m), Atwood number (At), and Reynolds number (Re), while considering tilt angle (θ) to be constant. Three-dimensional simulations were performed to study and compare the dynamics for the no viscosity differential case ($m = 1$) and a moderately high viscosity differential case ($m = 5$), while varying the other parameters. Also as we use single-relaxation time (SRT) based LBM, we investigate the problem at low to moderate Reynolds numbers. However, to operate the simulations at very high Reynolds numbers, one can use multiple-relaxation time (MRT) LBM which is more stable and accurate for high density ratios and high Reynolds nunbers Rahmati *et al*. (2014), Fakhari and Lee (2013). The findings are presented in the form of iso-surface/contour plots, axial/transverse variation of density and viscosity concentration and lengths of penetration.

The present LBM solver is implemented on graphics processing unit (GPU) to enhance the computational performance of LBM solver. Many researchers have developed and reported the implementation of LBM on single as well as multi- GPUs Kuznik *et al*. (2010), Vanka *et al*. (2011), Obrecht *et al*. (2013). As the implementation of LBM on GPU is easier and effective, it has become more popular since the last decade. It is a powerful tool that can executive massive parallel computations.

Thus the combination of this external hardware tool with the LBM solver produces dramatically high speed parallel simulations when compared to the CPU based LBM solver. In the present investigation, we perform GPU based LBM 3-D simulations to get a high computational speed up and a speed up of 25 times has been achieved over the corresponding fully CPU based LBM solver. We direct the readers to

Redapangu and Sahu (2013) for a detailed report on implementation of GPU on LBM using Nvidia CUDA programing and speed-up comparisons.

The rest of the following sections of the paper is organized as follows: A brief description of the present problem of consideration and the numerical method used are discussed in section 2. The results are presented and discussed in section 3. and section 4. provides the conclusions remarks.

2. PROBLEM FORMULATION

To study the 3-D flow dynamics of buoyancy-induced flow of two immiscible fluids, a three-dimensional rectangular coordinate system (X, Y, Z) is considered that represents the 3-D confined channel, with dimensions, *L* (length), *H* (height) and *W* (width), respectively. Here the height, *H* and the width, *W* are considered to be the same, i.e., *H* = *W* and the aspect ratio is *L*/*H* = 32. The 3-D channel considered here is inclined at a fixed angle θ = 60°, measured with the horizontal. The grid size considered is (1856 × 58 × 58) which is found to be an optimum grid size as evident from the discussions in section 3. of this paper.

The initial configuration of the system is shown in Fig. 1, where the upper part is filled with the heavier liquid ('1') whose density and viscosity are ρ_1 and μ_1, respectively. The lower part is occupied by a lighter liquid ('2') with density and viscosity, ρ_2 and μ_2, respectively. The interface separating the liquids is initially at the mid-length (X=*L*/2).

In this configuration, the flow behavior is due to the resultant of the inertial and the gravity forces. Here, as the geometry is inclined at an angle θ, the gravitational force vector has two non-zero components, g_X (= $g\sin\theta$) and g_Y (= $g\cos\theta$) that act in the negative axial and negative transverse directions, respectively. The dimensionless model parameters mainly considered in this study are:

1. Visocity ratio ($m = \mu_1/\mu_2$), that refers to the viscosity differential between the two liquids;
2. Atwood number ($At \equiv (\rho_2-\rho_1)/(\rho_2+\rho_1)$), which represents the density differential;
3. Reynolds number $Re(\equiv VH\rho_1/\mu_1)$.

Here, *V* is the characteristic velocity, $V = \sqrt{gH} = 0.08$. The effect of these parameters are investigated and presented in section 3., for a fixed tilt angle of θ = 60°. The other dimensionless parameters such as the Froude number (*Fr*) is defined as $Fr \equiv V/\sqrt{AtgH}$. In this study, it is a function of Atwood number only. Thus the investigation on Froude number has not been separately carried out in this work. Also, the surface tension force have been considered to be negligible in the present study, hence, the dimensionless Capillary number is not studied.

2.1 Numerical Method

The present problem is studied numerically using a two-phase lattice Boltzmann method (LBM), similar to that proposed and developed by Zhang *et al.* (2000). The method is explicit and second order accurate. It uses discrete lattice on which the simulations are performed. The current formulation is developed using D3Q15 (three-dimensional-fifteen velocity) lattice model (see Fig. 2). The evolution equations in the formulation contains two distribution functions (index distribution function (f_α) and the pressure distribution function (g_α)) which are used for tracking the interface and estimating the macroscopic properties of the fluids.

$$f_\alpha(\mathbf{x}+\mathbf{e}_\alpha\delta t, t+\delta t) - f_\alpha(\mathbf{x},t) = -\frac{f_\alpha(\mathbf{x},t) - f_\alpha^{eq}(\mathbf{x},t)}{\tau} - \frac{2\tau-1}{2\tau}\frac{(\mathbf{e}_\alpha-\mathbf{u}).\nabla\psi(\phi)}{c_s^2}\Gamma_\alpha(\mathbf{u})\delta t \quad (1)$$

$$g_\alpha(\mathbf{x}+\mathbf{e}_\alpha\delta t, t+\delta t) - g_\alpha(\mathbf{x},t) = -\frac{g_\alpha(\mathbf{x},t) - g_\alpha^{eq}(\mathbf{x},t)}{\tau} + \frac{2\tau-1}{2\tau}(\mathbf{e}_\alpha-\mathbf{u}).\left[\Gamma_\alpha(\mathbf{u})(F_s+\mathbf{G}) - (\Gamma_\alpha(\mathbf{u})-\Gamma_\alpha(0))\nabla\psi(\rho)\right]\delta t \quad (2)$$

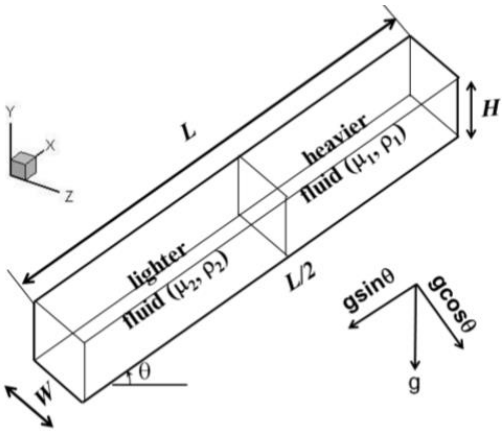

Fig. 1. 3-D confined inclined channel showing the initial configuration of the fluids separated by the initial interface at *X* = *L*/2.

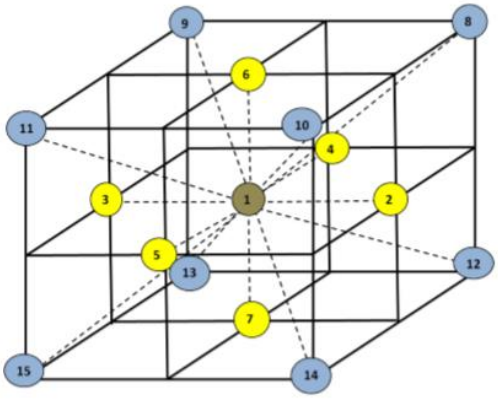

Fig. 2. D3Q15 lattice model showing 15 lattice directions.

Here x =(X,Y,Z) is the space vector, u =(*u*,*v*,*w*)

represents the three-dimensional velocity vector field; δt is the time step; , τ is the relaxation time, which is related to kinematic viscosity, ν as, $\nu = (\tau - 1/2)\delta t c_s^2$, where. $c_s^2 = 1/3$

For each lattice direction (a), the functions (fa) and (ga) at each position of space (vector x) and time (t) are to be estimated. The readers are referred to our previous article Redapangu *et al.* (2013) for the lattice velocities and the weighing coefficients of the D3Q15 model.

The Eqs. (1) and (2) are analogous to the macroscopic Navier-Stokes equations, continuity and volume fractions in the framework similar to the diffuse interface flow for interfacial flows. By Chapman-Enskog expansion Zhang *et al.* (2000), it can be shown that equations (1) and (2) are analogous to Eqs. (3), (4) and (5), as shown below.

$$\frac{\partial \phi}{\partial t} + \nabla.(\phi \mathbf{u}) = -\tau \nabla.\left[\frac{\phi}{\rho}\nabla p(\rho) - \nabla p(\phi)\right] \tag{3}$$

$$\frac{1}{\rho}\frac{\partial p}{\partial t} + \nabla.\mathbf{u} = 0 \tag{4}$$

$$\rho\left[\frac{\partial u}{\partial t} + (\mathbf{u}.\nabla)\mathbf{u}\right] = -\nabla p + \nabla.(\mu \nabla \mathbf{u}) + F_s + \mathbf{G} \tag{5}$$

The function $\Gamma_\alpha(u)$, in Eqs. (1 and 2) relates the weighing coefficients, lattice velocities and the macroscopic velocities as:

$$\Gamma_\alpha(\mathbf{u}) = t_\alpha\left[1 + \frac{\mathbf{e}_\alpha.\mathbf{u}}{c_s^2} + \frac{(\mathbf{e}_\alpha.\mathbf{u})^2}{2c_s^4} - \frac{\mathbf{u}^2}{2c_s^2}\right] \tag{6}$$

The equilibrium distribution functions, f_α^{eq} and g_α^{eq} can be estimated as:

$$f_\alpha^{eq} = t_\alpha \phi\left[1 + \frac{\mathbf{e}_\alpha.\mathbf{u}}{c_s^2} + \frac{(\mathbf{e}_\alpha.\mathbf{u})^2}{2c_s^4} - \frac{\mathbf{u}^2}{2c_s^2}\right] \text{ and} \tag{7}$$

$$g_\alpha^{eq} = t_\alpha\left[p + \rho c_s^2\left(\frac{\mathbf{e}_\alpha.\mathbf{u}}{c_s^2} + \frac{(\mathbf{e}_\alpha.\mathbf{u})^2}{2c_s^4} - \frac{\mathbf{u}^2}{2c_s^2}\right)\right], \tag{8}$$

The term $\psi(\phi)$ in Eq. (1) represents an equation that is responsible for phase segregation and incorporates intermolecular interactions for non-ideal gases or dense fluids. The Carnahan-Starling equation of state for $\psi(\phi)$, which describes non-ideal gases and fluids Carnahan and Starling (1969), Premnath and Abraham (2005) is given as:

$$\psi(\phi) = c_s^2\phi\left[\frac{1 + \phi + \phi^2 - \phi^3}{(1-\phi)^3} - 1\right] - a\phi^2, \tag{9}$$

Here, the parameter a represents the strength of molecular interactions. For an optimum value of $a > a_c$, (a_c = 3.53374, the critical value of Carnahan-Starling equation of state), the phase separation can be achieved. Therefore in the present study, a = 4 is chosen. The term $\psi(\rho)$ in Eq. (2) is given by $p - \rho c_s^2$. The terms $\nabla\psi(\phi)$ and $\nabla\psi(\rho)$ in Eq. (1) and Eq. (2), resepectively, are both descritzed using fourth-order compact scheme.

The evolution equations incorporates two force terms (Eq. (2), F_s, the surface tension force and G, the gravitational force. These can be estimated as below:

$$F_s = \kappa\phi\nabla\nabla^2\phi, \text{ and } \mathbf{G} = (\rho - \rho_m)g, \tag{10}$$

κ is a parameter that gives the magnitude of surface tension and $\rho_m \equiv (\rho_1+\rho_2)/2$. In the present study, only the gravitational forces are considered and the surface tension forces neglected.

Using the estimated distribution functions, the index function (ϕ), pressure (p) and the velocity field (u) can then be determined as:

$$\phi = \sum f_\alpha, \tag{11}$$

$$p = \sum g_\alpha - \frac{1}{2}\mathbf{u}.\nabla\psi(\rho)\delta t, \tag{12}$$

$$\rho\mathbf{u}c_s^2 = \sum \mathbf{e}_\alpha g_\alpha + \frac{c_s^2}{2}(\mathbf{F}_s + \mathbf{G})\delta t. \tag{13}$$

Now, the macroscopic properties, i.e., the density and the kinematic viscosity of the liquids at any instant can be estimated from the index function using the following equations:

$$\rho(\phi) = \rho_2 + \frac{\phi - \phi_2}{\phi_1 - \phi_2}(\rho_1 - \rho_2), \tag{14}$$

$$\nu(\phi) = \nu_2 + \frac{\phi - \phi_2}{\phi_1 - \phi_2}(\nu_1 - \nu_2), \tag{15}$$

Here, ν_1 and ν_2 represents the kinematic viscosities of the respective liquids. ϕ_1 = 0.02381 and ϕ_2 = 0.2508, which are the minimum and maximum values of the index function as shown by Zhang *et al.* (2000).

2.2 Implementation of Boundary Conditions.

Acccurate implementation of boundary conditions is the main important issue in LBM. While there are many proposals on the implementation of boundary conditions, in the present work, the hydrodynamic boundary conditions based on the ghost fluid approach Sahu and Vanka (2011) are applied to simulate the boundaries and the equilibrium distribution functions. Although the bounce back boundary condition can be applied directly for this geometry, it is to be noted that it is only first-order accurate. While improvements have also been available to make the bounce back boundary conditions more accurate, the author prefers to apply the hydrodynamic boundary conditions, the approach first proposed by Noble *et al.* (1995). With hydrodynamic boundary conditions, one could achieve 2-order accuracy while using the simple no-slip conditions to find the missing particle distributions. In the present formulation, the most

straightforward hydrodynamic boundary conditions are implemented as proposed by He *et al.* (1999a), Guo *et al.* (2002). In this approach, streaming components are not used and all the distribution functions are first set to the equilibrium values, which can be obtained by using the velocities and densities at the walls. The non-equilibrium values are then extrapolated and added to get the instantaneous distribution functions. No-slip and no-penetration conditions are applied for velocities, zero derivative boundary conditions are used for index-function, pressure and density calculation. Mathematically, these conditions can be written as below:

Index function ϕ **:** Zero-derivative boundary condition. The wall is placed between the lattice points. Here, the subscript '*wall*' stands for the wall node for all *X*,*Y*,*Z* planes as shown in Fig.3.

$$\phi_{wall} = \phi_{wall\pm1}, \tag{16}$$

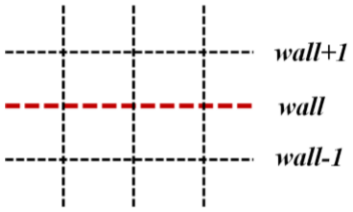

Fig. 3. Grid near the wall.

That means, for all the 3-spacial directions,

$$for \quad i = 1, nx; \quad j = 1:ny; \quad and \quad k = 1:nz;$$

we can write as;

$$\phi_{1,j,k} = \phi_{2,j,k}; \quad \phi_{nx,j,k} = \phi_{nx-1,j,k};$$
$$\phi_{i,1,k} = \phi_{i,2,k}; \quad \phi_{i,ny,k} = \phi_{i,ny-1,k};$$
$$\phi_{i,j,1} = \phi_{i,j,2}; \quad \phi_{i,j,nz} = \phi_{i,j,nz-1};$$

where *nx*, *ny* and *nz* are number of lattice points in the *X*, *Y* and *Z* directions, respectively.

Velocities: Velocities are mirror reflected to impose no slip and no penetration conditions. Mathematically, we can write as;

$$u_{wall} = \frac{u_{wall+1} + u_{wall-1}}{2}; \tag{17}$$

$$v_{wall} = \frac{v_{wall+1} + v_{wall-1}}{2} \tag{18}$$

$$w_{wall} = \frac{w_{wall+1} + w_{wall-1}}{2} \tag{19}$$

u_{wall}, v_{wall}, w_{wall} represents the respective velocity components at the walls. Here, $u_{wall} = v_{wall} = w_{wall}=0$, *Thus, for* $i = 1,nx$; $j = 1,ny$ *and* $k = 1,nz$; we can write as;

$u_{1,j,k} = -u_{2,j,k}$; $u_{nx,j,k} = -u_{nx-1,j,k}$;

$v_{1,j,k} = -v_{2,j,k}$; $v_{nx,j,k} = -v_{nx-1,j,k}$;

$w_{1,j,k} = -w_{2,j,k}$; $w_{nx,j,k} = -w_{nx-1,j,k}$

Index distribution function (*f*): The non-equilibrium values are extrapolated and added to get the instantaneous distribution functions.

$$f_{wall} = f^{eq}_{wall} + f^{eq}_{wall\pm1} \tag{20}$$

Thus, for $i = 1,nx$; $j = 1,ny$ *and* $k = 1,nz$; we can write as;

$$f_{1,j,k} = f^{eq}_{1,j,k} + f^{neq}_{2,j,k}; \quad f_{nx,j,k} = f^{eq}_{nx,j,k} + f^{neq}_{nx-1,j,k},$$

$$f_{i,1,k} = f^{eq}_{i,1,k} + f^{neq}_{i,2,k}; \quad f_{i,ny,k} = f^{eq}_{i,ny,k} + f^{neq}_{i,ny-1,k},$$

$$f_{i,j,1} = f^{eq}_{i,j,1} + f^{neq}_{i,j,2}; \quad f_{i,j,nz} = f^{eq}_{i,j,nz} + f^{neq}_{i,j,nz-1},$$

Pressure and pressure function (g): Pressure is extrapolated with zero derivative boundary condition. Thus at walls,

$$\rho_{wall} = \rho_{wall\pm1}, \tag{21}$$

Thus, for $i = 1,nx$; $j = 1,ny$ *and* $k = 1,nz$; we can write as;

$p1,j,k = p2,j,k$; $\quad pnx,j,k = pnx-1,j,k$,

$pi,1,k = pi,2,k$; $\quad pi,ny,k = pi,ny-1,k$,

$pi,j,1 = pi,j,2$; $\quad pi,j,nz = pi,j,nz-1$.

The pressure calculated here is used to evaluate the equilibrium pressure distribution function 'g'.

Density and ψ: The density is evaluated from the value of ϕ, which is extrapolated with zero derivative condition. $\psi(\equiv p-\rho RT)$ is evaluated at all the lattice points including the boundary points using appropriate boundary values of *p*.

The present LBM solver is further implemented on a graphics processing unit (GPU) to accelerate the computational efficiency. Performing simulations on GPU is very helpful mainly for three-dimensional simulations involving immiscible fluids as they demand high domains and thus are computationally highly expensive. With the implementation of LBM on GPU, a significantly considerable speedup has been achieved (25 times). For GPU implementation and speed-up comparisons, the readers are referred to our previous work Redapangu and Sahu (2013). All the 3-D simulations presented here were performed on the NVIDIA Tesla Kepler K10 graphics card that features two Kepler GPUs each of 8GB onboard memory. The present 2-phase LBM solver is validated and verified with the benchmark single phase 2D Rayleigh-Taylor problem which is more approriately related to the present investigation. Thus, we refer the readers to Sahu and Vanka (2011) for detailed validation of the LBM code.

3. RESULTS AND DISCUSSION

3.1 Grid Convergence Test:

To check the grid convergence of the present GPU

based LBM code, different grid sizes are considered and the physical behavior of the fluid flow are compared with respect to each grid size. The grid points used in this study are (1600×50×50), (1856 × 58 × 58) and (2112 × 66 × 66) in the (X, Y, Z) planes, respectively, with an aspect ratio L/H = 32. To show the grid independence, the spatio-temporal diagrams of $\int_0^H \phi dY$ in time versus X−plane are compared for different grid points as shown in Fig. 4. Rest of the common parameter values are At = 0.05, m = 1 and Re = 500. The spatio-temporal diagram of $\int_0^H \phi dY$ in time versus X−plane contains two regions, red and blue, indicating the regions of the heavier liquid and the lighter liquid, respectively, that are separated by a sharp interface (green region). Qualitative comparison of Fig. 4(a), (b) and (c) shows that the three contour plots look identical; that means the flow behavior on each of the considered grids is identical. To estimate the grid convergence quantitatively, the average velocity of the upper heavier liquid (V_1) and the bottom lighter liquid (V_2) are measured as they move into the regions of one another. The slope of the dashed line represents the velocity of each of the liquids. These velocities are tabulated in Table 1 for the three grids considered. It can be seen that the values are in good agreement and are within a tolerance of less than 0.1 %. Therefore, it can be concluded that the grid convergence is achieved and the rest of the simulations are performed using (1856×58×58) grid, treating it as an optimum grid size.

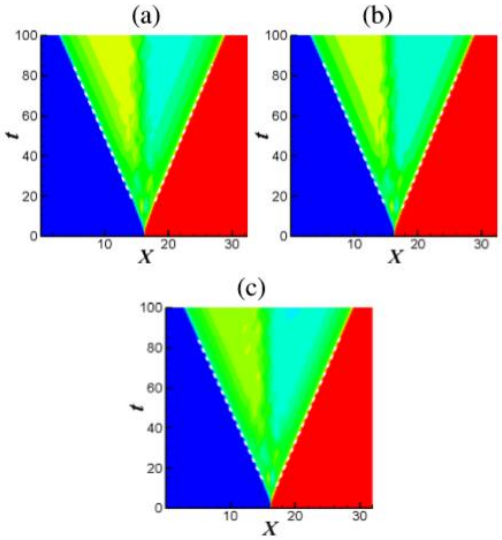

Fig. 4. Spatio-temporal diagram of $\int_0^H \phi dY$ in time versus X−plane for different grid points where (a) (1600 × 50 × 50),(b) (1856 × 58 × 58) and (c) (2112×66×66) for At =0.05, m=1 and Re=500.

3.2 Effect of Parameters on flow Dynamics:

The spatio-temporal evolution of the isosurface of the index function (ϕ) at the interface of the two

Table 1 Velocities of the heavier liquid (V1) and the lighter liquid (V2) for different grid densities for the parameters same as those of Fig. 4

Grid	V_1	V_2
1600×50×50	7.1715	7.6112
1856×58×58	7.1709	7.6126
2112×66×66	7.1704	7.614

liquids is shown in Fig. 5 for the simulation domain of (1856×58×58) grid. The rest of the parameters are the same as those of Fig. 4. This set of parameters represents a situation of the lock-exchange flow of two iso-viscous liquids, wherein the upper liquid is heavier than the lower liquid. Here, the flow is the resultant of the gravitational and the inertial forces. Mainly, as the channel is tilted, the gravitational force contains two non-zero components; the axial component of gravity, g_X(= $g\sin\theta$) and the transverse component of gravity, g_Y(= $g\cos\theta$), both acting in the negative X and Y directions, respectively. The axial component of gravity causes the downward motion of the heavier liquid, whereas the transverse component of gravity induces the segregation of the liquids. Therefore, as the time progresses, the upper heavier liquid because of the axial component of gravity moves downward into the region of the lighter liquid, while displacing it to move towards the upper region. Likewise, the two liquids try to interpenetrate into the regions of one another as seen in the Fig. 5. This movement makes the interface between the two liquids to become unstable leading to the formation of Kelvin-Helmholtz (KH) instabilities. The movement of the fingers and the formation of KH instabilities can be more clearly seen in Fig. 6, wherein the spatio-temporal evolution of the contours of the index function ϕ in the $X-Y$ plane of the three dimensional channel at $Z = W/2$ is presented for the same parameters as those of Fig. 5. As the time progresses, the two fluids penetrate into the regions of one another. The formation and the development of the KH instabilities can be seen at the earlier simulation times. However, these instabilities become weaker at later times and the flow seems to become more stabilized.

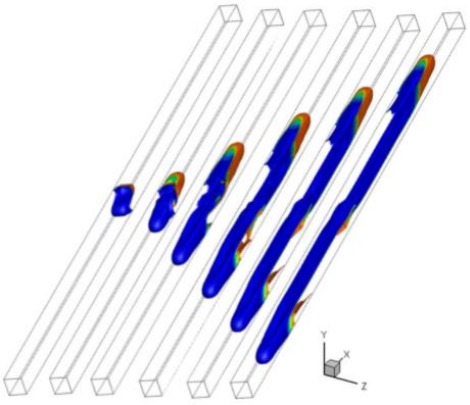

Fig. 5. Evolution of the isosurface of ϕ at the interface at different simulation times, t = 5, 10, 20, 30, 40, and 50, respectively, from left to right. The parameters are At = 0.05, m = 1, and Re=500.

For the same parameters of Fig. 5, 2-D simulations are carried out and are compared with the ϕ contours obtained in $X-Y$ plane of the 3-D channel as shown in Fig. 6. For the same set of parameters, the contours of index function obtained in 2-D counterpart are shown in Fig. 7. Similar comparison is presented in our previous work Redapangu and Sahu (2013). Upon comparison of Fig. 6 and Fig. 7, it can be observed that more small scale structures are clearly seen in two-dimensional simulation which are not evident in the 3D counterpart. Whereas, for the same parametric values, more stable mixing with different structure of instabilities is identified in 3D as evident from Fig. 6. Also, the instabilities appear more at the central portion of the 3D channel and smooth long fingers are seen towards both the ends of the channel. We also observe that the three-dimensional instabilities are more coherent than that of the two-dimensional counterparts. Close inspection of the coutours in both 2D and 3D studies concludes that for the same set of parameters, more stable and long fingers can be achieved in 3-D which were proved in agreement with the findings of Hallez and Magnaudet (2008), Oliveira and Meiburg (2011). Thus, it is necessary to investigate three-dimensional simulations for new insights as different structural behavior is observed. Therefore, in the sections below, we present the effect of different parameters on flow dynamics in the 3D channel.

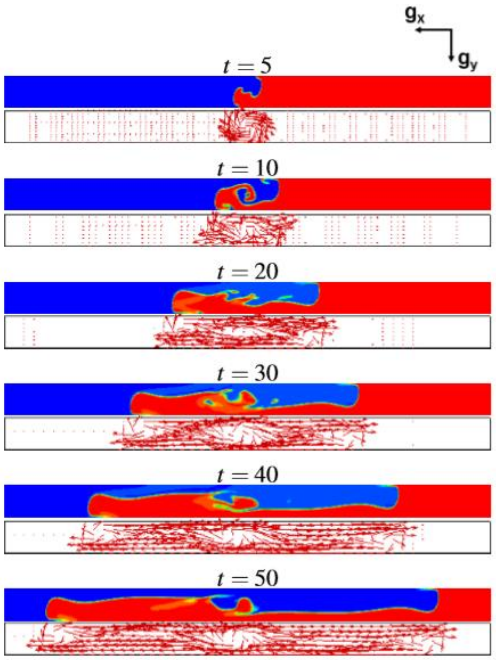

Fig. 6. Spatio-temporal evolution of the contours of the index function ϕ at different times in the $X-Y$ plane at $Z = W/2$ for the parameters same as that of Fig. 5. The panel shown below are the velocity vector directions.

To study the effect of viscosity ratio on flow dynamics in 3D channel, two cases are considered, m = 1 and m = 5. m = 1 represents the situation of iso-viscous fluids penetrating into the regions of one another. Whereas m = 5, indicates the situation where upper fluid is more viscous than the lower fluid. That means more viscous fluid penetrates into the region of less viscous fluid. Figure 8 shows the the contours of ϕ in the $X-Y$ plane for m = 5, rest of the parameters being the same as that of Fig. 6. The velocity vector directions are also shown in the panel below the contours. Comparison of Fig. 6 and Fig. 8 reveals that the interpenetration of the heavier and lighter fluids is slow when a higher viscosity differential exists between the fluids. That means the front velocities are lower for higher viscosity ratios. Further, the KH instabilities becomes weaker as the viscosity ratio increases as seen in Fig. 8 that more stable fingers are observed for m = 5. But by intuition, it can be expected that as the viscosity ratio increases, the instabilities increases and hence, the interpenetration increases. However, this is true only for m < 1, which represents the case of less viscous upper fluid penetrates into the more viscous lower fluid. This situation is an unstable configuration that leads to the formation of viscous instabilities more commonly known as viscous fingering Homsy (1987), Sahu *et al.* (2009). In such a situation, the formation of instabilities enhances the axial velocity of the two fluids and hence the interpenetration. But the situation considered here (m = 5) is fundamentally opposite to this, i.e; m > 1, where more viscous fluid penetrates into the region of less viscous fluid. This is a stable configuration. In such a case, the flow becomes more stable with increase in viscosity ratio, hence the interpenetration is slower. The same effect had been observed in case of 2-D simulations of lock-exchange flow of immiscible fluids carried out by Redapangu *et al.* (2012a).

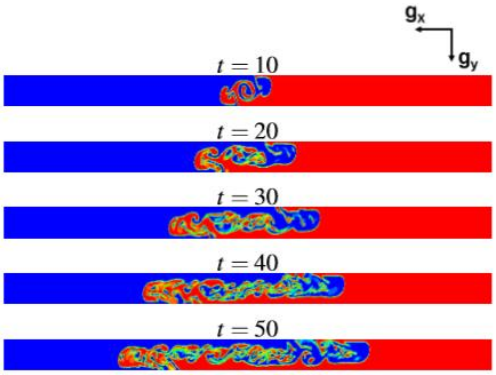

Fig. 7. Spatio-temporal evolution of the contours of the index function ϕ obtained in the two-dimensional simulation for the same parameters as that of Fig. 6.

To see the effect of Atwood number on flow dynamics, the spatio-temporal evolution of the contours of the index function ϕ in the $X-Y$ plane along with the velocity vectors are plotted for two different Atwood numbers. Figure 9 and Fig. 8 shows this for At = 0.01 and At = 0.05, respectively for m = 5 and Re = 500. It can be clearly observed from Fig. 9 and Fig. 8 that when the Atwood number is increased

from 0.01 to 0.05, the front velocities of the fingers increased because of the increase in the density contrast. Close inspection of Fig. 9 and Fig. 8 also reveals that the KH instabilities increases as the Atwood number increases. This effect is also true in 2-D simulations of the same problem Sahu and Vanka (2011).

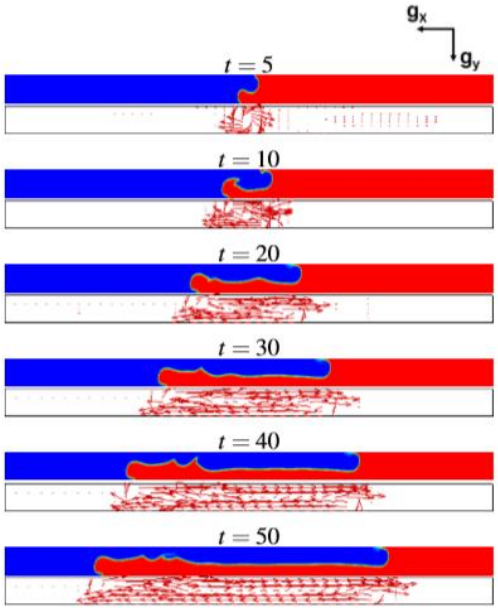

Fig. 8. Spatio-temporal evolution of the contours of the index function ϕ along with the velocity vectors at different times in the $X-Y$ plane at $Z=W/2$ for the parameters same as that of Fig. 5 but for m = 5.

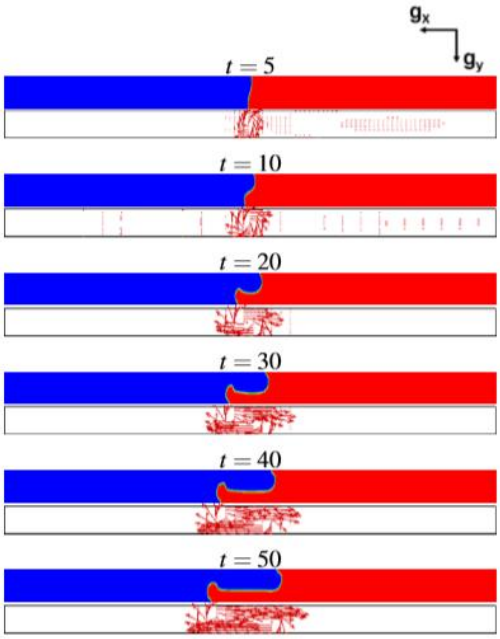

Fig. 9. Spatio-temporal evolution of the contours of the index function ϕ along with the velocity vectors at different times in the $X-Y$ plane at $Z=W/2$ for the parameters same as that of Fig.8 but for At = 0.01.

Next, we present the axial and the transverse variation of average density concentration across the channel for different parameters. The density concentration can be defined as $C \equiv (\rho - \rho_2)/(\rho_1 - \rho_2)$. Figure 10 shows the evolution of the axial variation of depth-averaged concentration, $\bar{C}_{YZ} = \frac{1}{HW}\int_0^W \int_0^H CdYdZ$ and the transverse variation axially-averaged concentration, $\bar{C}_{XZ} = \frac{1}{LW}\int_0^W \int_0^L CdXdZ$ for two different viscosity ratios (m). The other common parameters are At = 0.05 and Re = 500. Figure 10((a), (b)) corresponds to m = 1 and Fig. 10 ((c), (d)) corresponds to m = 5. The comparison of Fig. 10 (a), (c) which shows the variation of $\bar{C}_{YZ}$ along the axial direction for m = 1 and m = 5, respectively, reveals that the $\bar{C}_{YZ}$ profiles become more complex when a high viscosity gradient exists between the liquids. This complexity indicates the appearance of instabilities which are seen for iso-viscous liquids only at the initial times. In the studies of Redapangu *et al.* (2012a), the axial variation of depth-averaged concentration was observed to be more complex in 2-D simulations. Figure 10 (a), (c) also reveals that the interpenetration of fingers in the axial direction is more strong for m = 1 than that for m = 5. However, $\bar{C}_{XZ}$ profiles are more coherent and slightly asymmetric due to the segregation effect of the transverse gravitational component.

Figure 10 is compared to Fig. 11 where a smaller Atwood number is used (At = 0.01), the rest of the parameters being the same. $\bar{C}_{YZ}$ profiles reveal that for a smaller Atwood number, the axial interpenetration is lesser than that for both m = 1 (Fig. 11 (a)) and m = 5 (Fig. 11 (c)) when compared to Fig. 10 (a), (c). Also the small scale structures which are found to develop at earlier time levels are found to decrease as the At decreases. Hence this is also in agreement with the observations in Fig. 9 and Fig. 8 that with the decrease in Atwood number the intensity of instabilities decreases and also the axial interpenetration decreases. Also, Fig. 11 (a),(b) are comparable with *Fig.16 (c,d)* of Sahu and Vanka (2011). This comparison also reveals that the intensity of instabilities is high in 2-D flows than that of 3-D flows. This is because, the 2D currents create more coherent vortices and are stronger than their 3D counterparts. These coherent Kelvin-Helmholtz vortices become highly intense and live longer in 2D flows. While in 3D flows, the geometrical confinement created by the azhimuthal walls stabilizes the disturbances of smaller wavelenghts, thereby breaking the 2D coherent structures. Thus, the 3D instabilities are less intense and enable larger front velocities than 2D vortices as observed previously by many reasearchers Hallez and Magnaudet (2008), Oliveira and Meiburg (2011), Redapangu and Sahu (2013), Redapangu *et al.* (2013).

3.3 Effect of Parameters on Mixing Characteristics:

The interpenetration and the mixing characteristics

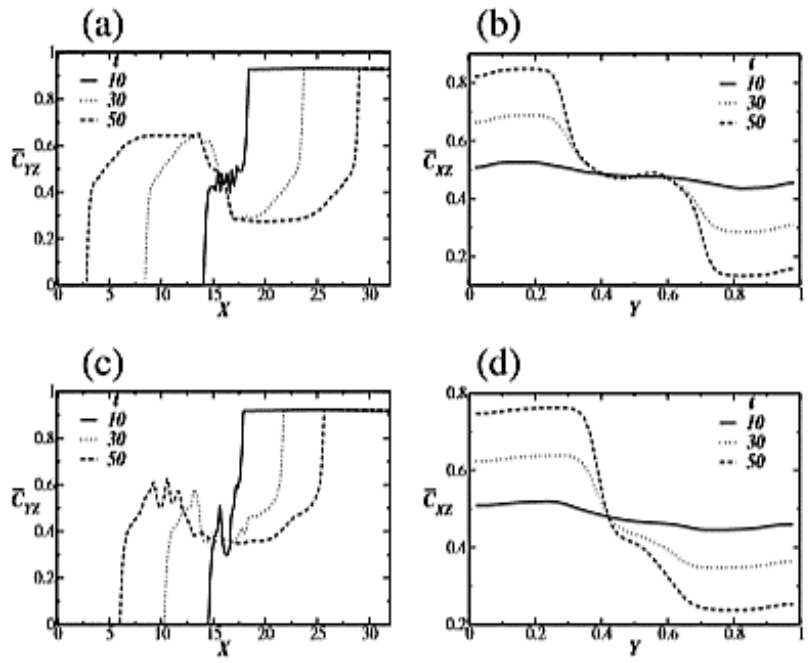

Fig. 10. Evolution of the axial variation of depthaveraged concentration ($\bar{C}_{YZ}$) and the transverse variation axially-averaged concentration ($\bar{C}_{XZ}$) for *m* = 1 ((a), (b)) and *m*=5 ((c), (d)), respectively. The other parameters are *At* = 0.05 and *Re* = 500.

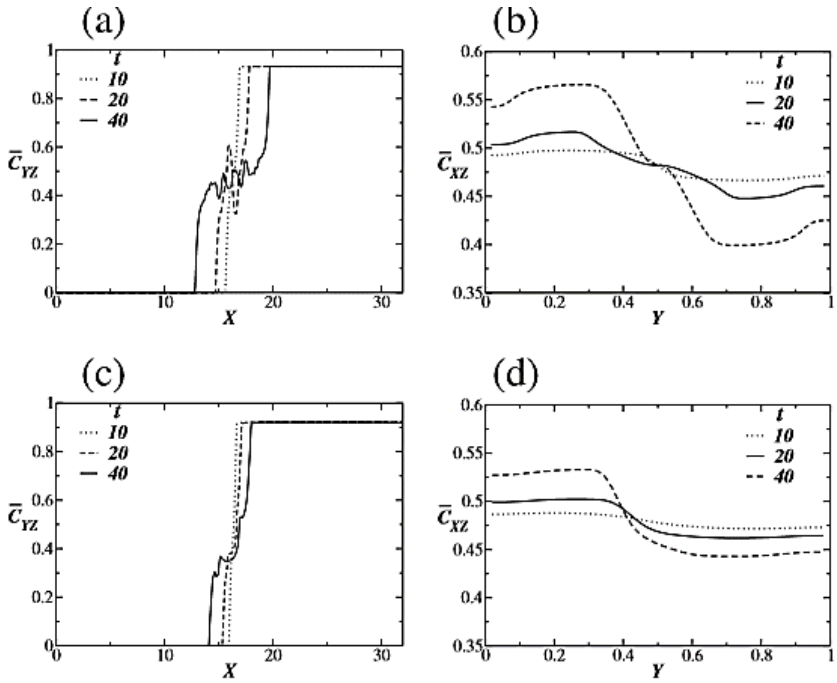

Fig. 11. Evolution of the axial variation of depth-averaged concentration ($\bar{C}_{YZ}$) and the transverse variation axially-averaged concentration ($\bar{C}_{XZ}$) for *m* = 1 ((a), (b)) and *m*=5 ((c), (d)), respectively. The other parameters are *At* = 0.01 and *Re*=500.

of the liquids in lock-exchange situation is then investigated. For this, the temporal variation of the location of fingers in the region above the initial interface (X_{locl}) and the region below the initial interface (X_{loch}) is plotted (Fig. 12) for different viscosity ratios (*m*) and Atwood numbers (*At*) for *Re* = 500. Here, X_{locl} refers to the location of the lighter liquid which moves towards the upper region above

the initial interface. Likewise, X_{loch} refers to the location of the heavier liquid which moves towards the lower region below the initial interface. (X_{loch}) and (X_{locl}) are both non-dimensional lengths which are non-dimensionalized with the height of the channel (H). It is clearly observed from Fig. 12 that higher interpenetration occurs for lower viscosity ratio and higher Atwood number. Also, it can be seen that the location of fingers in the upper and the lower regions are closely symmetric at all the simulation times.

Next, the length of the fingers that interpenetrate into each of the regions are measured. It can be called as the length of penetration (Lp^*), a dimensionless quantity wherein ($Lp^* = Lp/L$). Lp refers to the total length of the penetration of the fingers of the heavier and the lighter fluid as shown in the Fig. 13 (b) and L is the length of the channel. The measurement of (Lp^*) considers only axial penetration, the penetration in the transverse direction are not taken into consideration. Figure 13 (a) shows the variation of the length of penetration (Lp^*) for different viscosity ratios (m) and Atwood numbers (At). For all the parametric combinations considered here, the variation is found to be linear. The faster finger penetration is found for m = 1 and At = 0.05. That means when the liquids are of iso-viscous and when the heavier liquid is much heavier than the lighter liquid, the interpenetration occurs more rigorously. For the same Atwood number, if the heavier liquid is more viscous than the lighter liquid, it can be seen that the length of penetration is slightly lesser than that obtained for iso-viscous case.

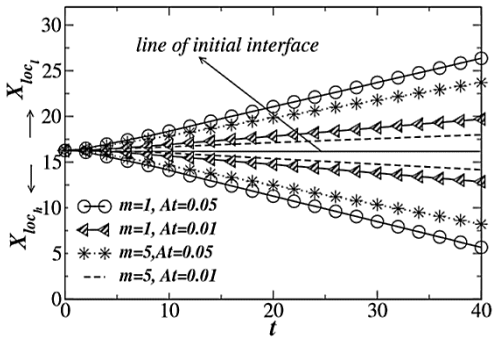

Fig. 12. Temporal variation of the location of the fingers in the region above the initial interface (X_{locl}) and region below the initial interface (X_{loch}) for different viscosity ratios (m) and Atwood numbers (At) for Re = 500.

Lastly, to study how Reynolds number effects the length of penetration, consider the case of m = 1 and At = 0.05, for which higher length of penetration is achieved as evident from Fig. 13(a) and test the behavior with different Reynolds numbers. Figure 14 shows this for Re = 100, 500 and 1000. It is observed that at all the time levels, higher Lp^* is achieved for Re = 500 and there is a slight decrease in Lp^* for Re = 1000. That means the axial interpenetration of two fluids increases till Re = 500 and then decreases, indicating a non-monotonic variation for this set of parameters. The non-monotonic effect of Re on the front velocity had also been observed earlier by Sahu and Vanka (2011) at a higher At. To see the transverse interpenetration, the contours of the index function ϕ in the $Y - Z$ plane at the mid-length of the geometry ($X = L/2$) are shown in Fig. 15 for Re = 500 and 1000 at various simulation times. It is evident that at all the time levels, mixing in the transverse direction is more vigorous for Re = 1000 than that for Re = 500. Thus for this set of parameters as the Reynolds number increases, mixing in the axial direction decreases, whereas the transverse interpenetration increases. The reason for this behavior is that at higher Reynolds number, due to the development of Kelvin-Helmholtz instabilities more complex flow structures appear that lead to higher transverse interpenetration. This behavior was also observed by Sahu and Vanka (2011) for 2-D buoyancy flows who depicted the reason for this behavior as "*increasing the value of Reynolds number from Re =300 to 1500, leads to the rapid development of Kelvin-Helmholtz instabilities which in turn lead to complex dynamics and intricate flow patterns. These KH type instabilities accompanying the flow promote a significant level of transverse interpenetration*". This is also evident from Fig. 16 that more complex structures in ($\bar{C}_{YZ}$) profiles are seen for Re=1000 than that for Re=500 at all the simulation times showed. These complex structures indicate the development of Kelvin-Helmholtz instabilities leading to 'higher transverse interpenetration' which can be referred to as 'rapid mixing' in the transverse direction.

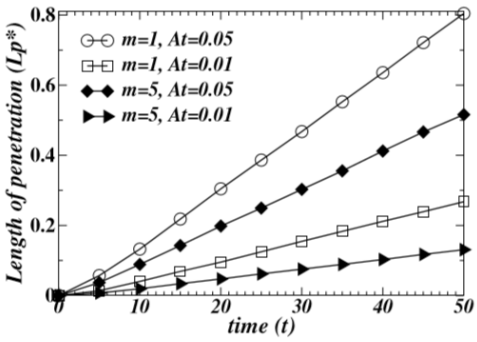

(a)

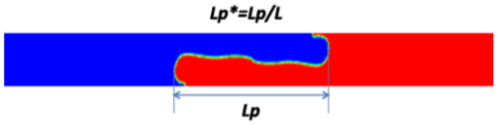

(b)

Fig. 13. (a) The variation of the length of penetration (Lp^*) for different viscosity ratios (m) and Atwood numbers (At) for Re = 500, (b) contour showing the measurement of Lp^*.

4. CONCLUSIONS

Three-dimensional lattice Boltzmann simulations

were performed to study the buoyancy-driven flow of two immiscible liquids of varying density and viscosity. The implementation of LB solver on graphics processing unit is found to be very promising and useful mainly for immiscible 3-D simulations as they require high computational domains. The present study is mainly focused on studying the flow and the mixing characteristics obtained in a three-dimensional confined inclined channel. Mainly the effects of viscosity ratio (*m*), Atwood number (*At*) and Reynolds number (*Re*), on the density profiles and lengths of interpenetration had been presented. The three-dimensional characteristics are found to be different to that of two-dimensional flows. Reynolds number had a non-monotonic effect on the axial length of penetration (Lp^*). Larger axial interpenetration lengths are observed for iso-viscous liquids with higher density gradient for an optimum value of *Re* = 500. An increase in Reynolds increased the intensity of KH instabilities and thus higher transverse interpenetration is observed for *Re* = 1000.

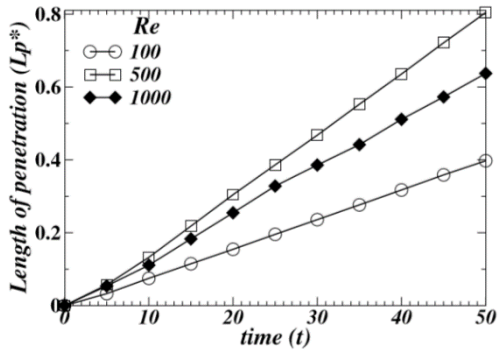

Fig. 14. Temporal variation of the length of penetration (Lp^*) for different Reynolds numbers for *m* = 1 and *At* = 0.05.

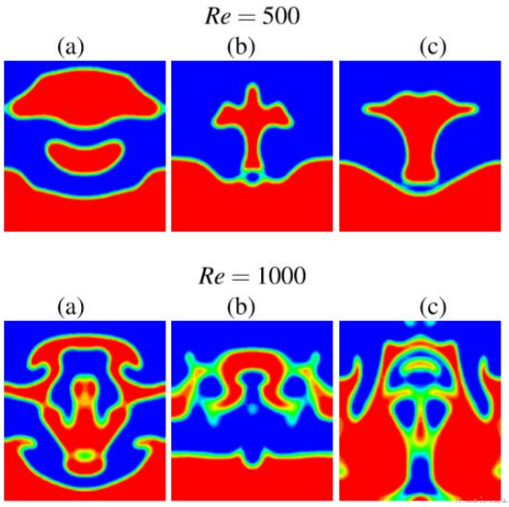

Fig. 15. Contours of the index function φ in the *Y* −*Z* plane at *X* = *L*/2 for *m* = 1 and *At* = 0.05. (a), (b) and (c) in the panel correspond to times *t* = 10,30 and 50, respectively.

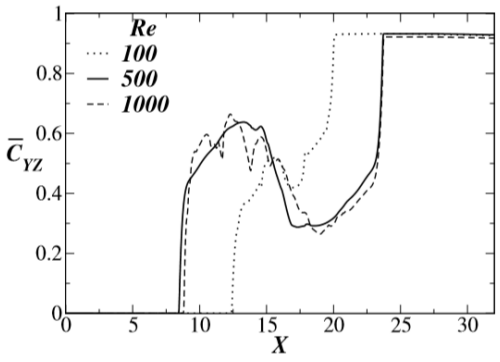

(a)

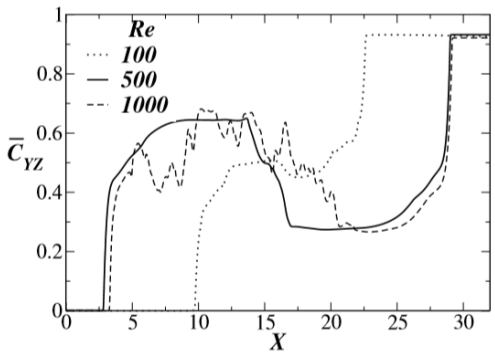

(b)

Fig. 16. Evolution of the axial variation of depth-averaged concentration ($\bar{C}_{YZ}$) for different Reynolds number (*Re*) at simulation times (a) *t* = 30 and (b) *t* = 50. The other parameters are *m* = 1 and *At* = 0.05.

ACKNOWLEDGMENTS

All the 3-D simulations performed in this work are carried out at the 'High-performance Computational lab' in the Department of Chemical Engineering at Indian Institute of Technology Hyderabad, India (IIT-H). The support from IIT-H is gratefully acknowledged. Prasanna R. Redapangu is highly thankful to Dr. Kirti Chandra Sahu, IITH for his valuable inputs and suggestions towards improving the quality of the work.

REFERENCES

Benjamin, T. B. (1968). Gravity currents and related phenomena. *Journal of Fluid Mechanics*31, 209– 248.

Birman, V. K., B. A. Battandier, E. Meiburg and P. F. Linden (2007). Lock-exchange flows in sloping channels. *Journal of Fluid Mechanics* 577, 53–77.

Birman, V. K., J. E. Martin and E. Meiburg (2005). The non-boussinesq lock-exchange problem. Part 2. High-resolution simulations. *Journal of Fluid Mechanics* 537, 125.

Carnahan, N. F. and K. E. Starling (1969). Equation of state for non-attracting rigid spheres. *Journal*

of Chemical Physics 51, 635–636.

Chang, Q. and J. I. D. Alexander (2006). Application of the lattice Boltzmann method to two-phase Rayleigh-Benard convection with a deformable interface. *Journal of Computational Physics* 2012, 473–489.

Chen, S., D. Martinez and R. Mei (1996). On boundary conditions in lattice Boltzmann methods. *Physics of Fluids* 8, 2527–2536.

Debacq, M., J. P. Hulin, D. Salin, B. Perrin, and E. J. Hinch (2003). Buoyant mixing of miscible fluids of varying viscosities in vertical tubes. *Physics of Fluids* 15(12), 3846–3855.

Debacq, M., V. Fanguet, J. P. Hulin, D. Salin and B. Perrin (2001). Self-similar concentration profiles in buoyant mixing of miscible fluids in a vertical tube. *Physics of Fluids* 13, 3097.

Ding, H., P. D. M. Spelt and C. Shu (2007). Diffuse interface model for incompressible two-phase flows with large density ratios. *Journal of Computational Physics* 226, 2078–2095.

Fakhari, A. and M. H. Rahimian (2009). Simulation of falling droplet by the lattice Boltzmann method. *Communications in Nonlinear Science and Numerical Simulations* 14, 3046–3055.

Fakhari, A. and M. H. Rahimian (2010). Investigation of deformation and breakup of a moving droplet by the method of lattice Boltzmann equations. *International Journal for Numerical Methods in Fluids* 64, 827–849.

Fakhari, A. and T. Lee (2013). Multiplerelaxation-time lattice boltzmann method for immiscible fluids at high reynolds numbers. *Physical Review E* 87, 023304.

Fernandez, J., P. Kurowski, P. Petitjeans and E. Meiburg (2002). Density driven unstable flows of miscible fluids in a Hele-Shaw cell. *Journal of Fluid Mechanics* 451, 239.

Guo, Z., C. Zheng and B. D. Shi (2002). An extrapolation method for boundary conditions in lattice Boltzmann method. *Physics of Fluids* 14, 2007–2010.

Hallez, Y. and J. Magnaudet (2008). Effects of channel geometry on buoyancy-driven mixing. *Physics of Fluids* 20, 053306(1–9).

Hallez, Y. and J. Magnaudet (2009). A numerical investigation of horizontal viscous gravity currents. *Journal of Fluid Mechanics* 630, 71–91.

He, X., R. Zhang, S. Chen and G. D. Doolen (1999a). On the three-dimensional Rayleigh-Taylor instability. *Physics of Fluids* 11(5), 1143– 1152.

He, X., S. Chen and R. Zhang (1999b). A lattice Boltzmann scheme for incompressible multiphase flow and its application in simulation of Rayleigh-Taylor instability. *Journal of Computational Physics* 152, 642–663.

Homsy, G. M. (1987). Viscous fingering in porous media. *Annual Review of Fluid Mechanics* 19, 271–311.

Kuznik, F., C. Obrecht, G. Rusaouen and J. J. Roux (2010). LBM based flow simulation using GPU computing processor. *Computers and Mathematics with Applications* 59, 2380–2392.

Lee, H. G. and J. Kim (2013). Buoyancy-driven mixing of multi-component fluids in twodimensional tilted channels. *European Journal of Mechanics - B/Fluids* 42, 37–46.

Li, P., C. Peng, P. Du, Y. Zhang, B. Dong and M. Ma (2019, 09). The investigation of viscous fingering phenomenon of immiscible fluids displacement by lattice Boltzmann method. *Canadian Journal of Physics*. 2020, 98(7), 650-659

Noble, D. R., J. G. Georgiadis and R. O. Buckius (1995). Direct assessment of lattice Boltzmann hydrodynamics and boundary conditions for recirculating flows. *Journal of Statistical Physics* 81, 17–33.

Obrecht, C., F. Kuznik, B. Tourancheau and J.J. Roux (2013). Multi-GPU implementation of the lattice boltzmann method. *Computers and Mathematics with Applications* 65, 252 – 261.

Oliveira, R. M. and E. Meiburg (2011). Miscible displacements in Hele-Shaw cells: three-dimensional Navier-Stokes simulations. *Journal of Fluid Mechanics* 687, 431–460.

Premnath, K. N. and J. Abraham (2005). Lattice Boltzmann model for axisymmetric multiphase flows. *Physical Review E* 71, 056706(1–17).

Rahmati, A. R. and A. Najjarnezami (2016). A double multi-relaxation-time lattice boltzmann method for simulation of magneto hydrodynamics natural convection of nanofluid in a square cavity. *Journal of Applied Fluid Mechanics* 9, 1201–1214.

Rahmati, A. R., M. Ashrafizaadeh and E. Shirani (2014). A multi-relaxation-time lattice boltzmann method on non-uniform grids for large eddy simulation of rayleigh-bnard convection using two sub-grid scale models. *Journal of Applied Fluid Mechanics* 7, 89 – 102.

Redapangu, P. R. and K. C. Sahu (2013, February). Three-dimensional LBM simulations of buoyancy-driven flow using Graphics processing units. In *National Conference on parallel computing technologies*, C-DAC, Bangalore. IEEE. Paper number 40.

Redapangu, P. R., K. C. Sahu and S. P. Vanka (2012a). A study of pressure-driven displacement flow of two immiscible liquids using a multiphase lattice Boltzmann approach. *Physics of Fluids 24*, 102110.

Redapangu, P. R., K. C. Sahu and S. P. Vanka (2013). A lattice Boltzmann simulation of two

immiscible liquids in a square duct. *ASME Journal of Fluids Engineering* 135, 121202(1–8).

Redapangu, P. R., S. P. Vanka and K. C. Sahu (2012a). Multiphase lattice Boltzmann simulations of buoyancy-induced flow of two immiscible fluids with different viscosities. *The European Journal of Mechanics - B/Fluids* 34, 105–115.

Séon, T., D. Salin, J. P. Hulin, B. Perrin and E. J.´ Hinch (2004). Buoyant mixing of miscible fluids in tilted tubes. *Physics of Fluids* 16, L103– L106.

Séon, T., D. Salin, J. P. Hulin, B. Perrin and´ E. J. Hinch (2005). Buoyancy driven front dynamics in tilted tubes. *Physics of Fluids* 17, 031702(1–4).

Séon, T., D. Salin, J. P. Hulin, E. J. Hinch and´ B. Perrin (2007b). Transient buoyancy-driven front dynamics in nearly horizontal tubes. *Physics of Fluids* 19, 123603(1–4).

Séon, T., J. P. Hulin, D. Salin, B. Perrin and E. J. Hinch (2006). From turbulent mixing to gravity currents in tilted tubes. *Physics of Fluids* 18, 091103.

Séon, T., J. Znaien, B. Perrin, E. J. Hinch,´ D. Salin and J. P. Hulin (2007). Front dynamics and macroscopic diffusion in buoyant mixing in a tilted tube. *Physics of Fluids* 19(12), 125105(1–7).

Sahu, K. C. and S. P. Vanka (2011). A multiphase lattice Boltzmann study of buoyancyinduced mixing in a tilted channel. *Computers & Fluids* 50, 199–215.

Sahu, K. C., H. Ding, P. Valluri and O. K. Matar (2009). Linear stability analysis and numerical simulation of miscible two-layer channel flow. *Physics of Fluids* 21, 042104(1–8).

Shan, X. and G. Doolen (1995). Multicomponent lattice-Boltzmann model with interparticle interaction. *Journal of Statistical Physics* 81, 379–393.

Shan, X. and H. Chen (1993). Lattice Boltzmann model for simulating flows with multiple phases and components. *Physical Review E* 47, 1815–1819.

Succi, S., R. Benzi and F. Higuera (1991). The lattice Boltzmann equationa new tool for computational fluid dynamics. *Physica D* 47, 219–30.

Vanka, S. P., A. F. Shinn and K. C. Sahu (2011, November 11-17). Computational fluid dynamics using graphics processing units: Challenges and Opportunities. In *Proceedings of the ASME 2011 International Mechanical Engineering Congress and Exposition*, Denver, Colorado, USA. ASME.

Wakale, A. B., K. Venkatasubbaiah and K. C. Sahu (2015). A parametric study of buoyancy-driven flow of two-immiscible fluids in a differentially heated inclined channel. *Computers & Fluids* 117, 54–61.

Wood, I. R. (1970). A lock exchange flow. *Journal of Fluid Mechanics* 42, 671–687.

Zhang, R., X. He and S. Chen (2000). Interface and surface tension in incompressible lattice Boltzmann multiphase model. *Computer Physics Communications* 129, 121–130.